Experimental estimation of transmissibility matrices for industrial multi-axis vibration isolation systems

Michiel A. Beijen [a,*], Robbert Voorhoeve [a], Marcel F. Heertjes [a,b], Tom Oomen [a]

[a] Eindhoven University of Technology, Department of Mechanical Engineering, Control Systems Technology Group, PO Box 513, 5600 MB Eindhoven, The Netherlands
[b] ASML Mechatronic Systems Development, 5504 DR Veldhoven, The Netherlands

ARTICLE INFO

ABSTRACT

Vibration isolation is essential for industrial high-precision systems to suppress external disturbances. The aim of this paper is to develop a general identification approach to estimate the frequency response function (FRF) of the transmissibility matrix, which is a key performance indicator for vibration isolation systems. The major challenge lies in obtaining a good signal-to-noise ratio in view of a large system weight. A non-parametric system identification method is proposed that combines floor and shaker excitations. Furthermore, a method is presented to analyze the input power spectrum of the floor excitations, both in terms of magnitude and direction. In turn, the input design of the shaker excitation signals is investigated to obtain sufficient excitation power in all directions with minimum experiment cost. The proposed methods are shown to provide an accurate FRF of the transmissibility matrix in three relevant directions on an industrial active vibration isolation system over a large frequency range. This demonstrates that, despite their heavy weight, industrial vibration isolation systems can be accurately identified using this approach.

© 2018 Elsevier Ltd. All rights reserved.

1. Introduction

Vibration isolators are widely used in high-precision systems, such as wafer scanners [1], scanning tunneling microscopes [2,3], and measurement systems in general [4,5]. These isolators are used to isolate machinery from floor and base frame vibrations. A key performance indicator is the transmissibility function [5,6]. For single-axis systems, the transmissibility function describes the transfer function from base frame vibrations to payload vibrations. For multi-axis systems, the transmissibility function is extended to a transmissibility matrix, where its performance metric is often posed in terms of scalar norms [6,7]. Amongst vibration isolation, the concept of transmissibility functions has a key interest in a wide range of applications, for example operational modal analysis [8,9], and operational transfer path analysis [10,11].

The frequency response function (FRF) of the transmissibility matrix can be estimated from experimental data by placing accelerometers or geophones on both the base frame and the isolated payload of the machine [12]. In, e.g., [6,13,14], several methods for transmissibility matrix measurements are developed where external shaker constructions are used to ensure that the base frame is sufficiently excited. This enables an accurate estimation of the FRF, both unbiased and with a small variance [15]. However, these methods are often not applicable because industrial machines are often too heavy for

commercially available shakers to support and excite the system. Moreover, in industry it is important to provide sufficiently accurate models on the one hand with the least-costly identification experiment on the other hand [16]. Therefore, estimation methods that allow the machine to perform under operating conditions are highly preferred. Such methods rely on environmental base frame excitations, e.g., floor vibrations [17]. These methods can result in a reasonable estimation, as long as the environmental vibrations provide sufficient spectral power in all relevant directions to obtain a sufficient signal-to-noise ratio (SNR). Available methods are restricted to those that can deal with random excitations, because the environmental vibrations are not known beforehand and are typically non-periodic. In this regard, spectral analysis is often used [18,19], which assumes that either the base frame or the payload excitation is measured free of noise. However, sensor noise on both the base frame and payload measurement leads to an error-in-variables identification problem [20,21], which may subsequently lead to biased estimates [22,23].

Several methods are proposed in literature to improve the estimation results for systems that can only be partly identified. A first example is output-only or operational modal analysis [8,9] which can provide eigenfrequencies and mode shapes, but does not give an FRF which represents an input–output relation. A second example is found in methods that augment FRF measurements with finite-element modeling, e.g., [24], but these methods need intervention regarding meshing, model order selection, and so on. A third example is frequency-based substructuring [25,26] in which separate parts of the system are identified independently and merged afterwards, but this method is sensitive for large uncertainty propagation errors [25]. Moreover, none of these methods provides a validation regarding the actual performance of the assembled system in closed-loop. The latter is important, since control loops might deteriorate performance due to changing system dynamics and noise amplification [27–29]. Therefore, none of these methods is further pursued in this paper.

Although vibration isolation is essential in high-tech equipment, there is a lack of a systematic approach to estimate the FRF of the transmissibility matrix for heavy-weight systems. The first contribution of this paper is to show a non-parametric identification method to estimate the FRF for such systems in multiple directions, where a combination of floor and shaker excitations is used to maximize the base frame excitation power. The second contribution is a method to evaluate the spectral power and directions of the base frame excitations, and how its result can be used for input design of the shaker excitation signals. In this respect, the proposed method can be seen as optimal input design [16]. A third contribution is given by the application of the identification and input design methods to a heavy-weight active vibration isolation system. This leads to an accurately estimated FRF of the transmissibility matrix in the frequency range of interest, i.e. between 1 and 100 Hz, and in three relevant directions. These results show that the presented methods, which are applicable for vibration isolation systems in general, are particularly suited for systems that are too heavy to be sufficiently excited by shakers during operating conditions.

The paper is organized as follows. The experimental setup and the transmissibility matrix are described in Section 2. The main problem considered in this paper is defined in Section 3. The non-parametric identification method is presented in Section 4, and the input excitation analysis and design method is presented in Section 5. The experimental results and validation are presented in Section 6, and the major conclusions are given in Section 7.

2. Active vibration isolation system

2.1. System description

The system used throughout this paper for validation purposes is the Active Vibration Isolation System (AVIS) shown in Fig. 1. The AVIS consists of two main parts: (i) an isolated payload of 289 kg, and (ii) a base frame (BF) that is supported by the floor. The payload and BF are connected by four isolator modules (IM). These isolator modules provide a low stiffness and
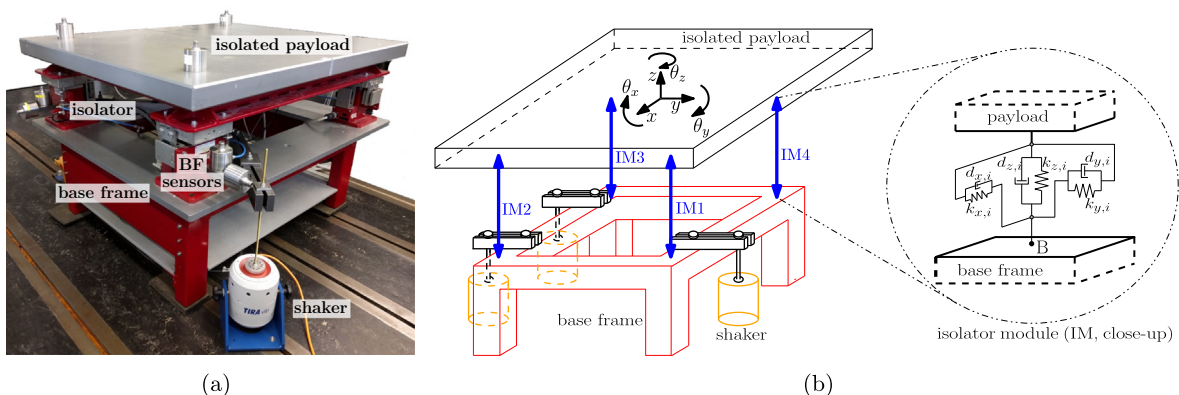

(a) (b)

Fig. 1. AVIS used for validation of the non-parametric identification method: (a) photograph, (b) schematic representation showing the base frame, payload, four isolator module locations, and three shaker locations.

damping through pneumatically controlled air mounts to obtain vibration isolation. At three of the four modules, horizontal and vertical accelerometers are placed to measure the absolute BF accelerations denoted by $\boldsymbol{u_1}(t) \in \mathbb{R}^6$. Moreover, three out of four modules contain horizontal and vertical accelerometers on the payload to measure the absolute payload accelerations denoted by $\boldsymbol{y_1}(t) \in \mathbb{R}^6$. Measurements of $\boldsymbol{u_1}$ and $\boldsymbol{y_1}$ are filtered with analogue band-pass filters from 0.1 Hz to 450 Hz to reduce aliasing, sensor noise, cross-talk, and drift. For ease of presentation, $\boldsymbol{u_1}$ and $\boldsymbol{y_1}$ are transformed to the same coordinate frame, i.e. the set of Cartesian coordinates in the center of gravity (CoG) of the payload, see Fig. 1b. To this end, both the BF and payload are considered as a rigid body, such that the BF motion is defined by $\boldsymbol{x_b}(t) = [x_b, y_b, z_b, \theta_{x,b}, \theta_{y,b}, \theta_{z,b}]^T$ and the payload motion is defined by $\boldsymbol{x_p}(t) = [x_p, y_p, z_p, \theta_{x,p}, \theta_{y,p}, \theta_{z,p}]^T$. In the absence of sensor noise, and only considering small displacements, the Cartesian coordinates are related to the measured signals through

$$\ddot{\boldsymbol{x}}_{\boldsymbol{b}}(t) = \mathbf{T_u}\boldsymbol{u_1}(t), \quad \ddot{\boldsymbol{x}}_{\boldsymbol{p}}(t) = \mathbf{T_y}\boldsymbol{y_1}(t), \tag{1}$$

with transformation matrices $\mathbf{T_u}, \mathbf{T_y} \in \mathbb{R}^{6 \times 6}$.

Three shakers providing vertical shaker forces $\boldsymbol{r}(t) \in \mathbb{R}^3$ are installed between the floor and the BF to increase the excitation level of the BF. The shaker locations are shown in Fig. 1b. Data acquisition is performed by a 14-bit real-time digital signal processor (DSP) running at $f_s = 2$ kHz.

2.2. The transmissibility matrix

The FRF of the $n_y \times n_u$ transmissibility matrix $\mathcal{T}(j\omega)$, with frequency $\omega \in \mathbb{R}$, defines the relation between a set of BF coordinates $\boldsymbol{x_b} \in \mathbb{R}^{n_u}$ and a set of payload coordinates $\boldsymbol{x_p} \in \mathbb{R}^{n_y}$ in the frequency domain. In general, a transmissibility matrix is not uniquely defined by $\boldsymbol{x_b}$ and $\boldsymbol{x_p}$ only, but also depends on the locations of the floor and shaker excitation sources $\boldsymbol{f}$ causing the responses measured at $\boldsymbol{x_b}$ and $\boldsymbol{x_p}$. This property is extensively investigated in, e.g., [10] for linear time-invariant (LTI) systems. In order to make $\mathcal{T}$ uniquely defined and independent of $\boldsymbol{f}$ in case of vibration isolation systems, the number of considered BF coordinates n_u must equal the number of transmission paths between the BF and the payload. Moreover, the BF sensors must be co-located with the attachment points of the transmission paths, for example, the vertical BF acceleration of each air mount must be measured at the point B in the IM close-up in Fig. 1b. By doing so, structural dynamics of the BF will not be involved in the transmission path from $\boldsymbol{x_b}$ to $\boldsymbol{x_p}$. Under these conditions, $\mathcal{T}$ becomes independent of BF dynamics and the locations of the excitation sources, such that $\mathcal{T}$ can be regarded as an input–output relation from $\boldsymbol{x_b}$ to $\boldsymbol{x_p}$, or

$$\boldsymbol{X_p}(\omega) = \mathcal{T}(j\omega)\boldsymbol{X_b}(\omega), \tag{2}$$

with $\boldsymbol{X_p}(\omega), \boldsymbol{X_b}(\omega)$ representing the payload and BF motion expressed in the frequency domain.

An expression for $\mathcal{T}(j\omega)$ could be either obtained from parametric first-principles modeling or from measured frequency response data. A first-principles model for the transmissibility matrix is derived in Appendix A. In this model, the payload is considered as a rigid body while the air mounts are described using the three-spring-damper model as shown in Fig. 1b. As such, there are twelve transmission paths, i.e. four air mounts each containing three spring-damper connections between the BF and payload. This can be reduced to six transmission paths by considering the BF as a rigid body, such that all twelve attachment points of the transmission paths only depend on the six rigid-body degrees of freedom of the BF. Due to the modeling assumptions this model is only valid at low frequencies where no structural dynamics or air mount dynamics occur. The model is therefore not sufficient to provide an accurately estimated FRF of the transmissibility matrix in the full frequency range of interest between 1 and 100 Hz. As such, the model will only be used for input design of the shaker signals, and to validate FRF measurements of the transmissibility matrix obtained from experiments at low frequencies.

3. Problem definition

The aim of this paper is to develop a general identification approach to estimate the transmissibility matrix $\mathcal{T}$ for industrial systems running under operating conditions, such as the system in Fig. 1. More specifically, the key interest is to measure the FRF $\mathcal{T}(j\omega)$ in a broad frequency of interest, which is typically 1–100 Hz for industrial high-precision machines, and in multiple directions. The main challenge in the identification of $\mathcal{T}$ lies in the fact that excitation of $\boldsymbol{X_b}$ is limited due to physical constraints. Environmental vibrations always excite the BF, but these excitations are uncertain in spectral power and directions. Nevertheless, these vibrations are exploited as useful excitation signal. In addition, these excitations can be augmented with shaker excitations to sufficiently excite the BF in the remaining directions and frequencies that are not sufficiently excited by the environment. These shaker excitations are designed carefully to obtain sufficient excitation power with minimum experiment cost.

4. Non-parametric system identification

In this section, the non-parametric identification method to identify the FRF of $\mathcal{T}$ is presented. Spectral analysis is used to simultaneously benefit from environmental floor and shaker excitations [30]. Bias analysis and 95% confidence regions are presented to determine the quality of the measured FRF.

Fig. 2 shows the block diagram used for non-parametric system identification. The goal is to identify $\mathcal{T}$. Signals $\boldsymbol{u}_1$ and $\boldsymbol{y}_1$ represent the BF and payload motions in sensor coordinates as described in Section 2. Signal $\boldsymbol{u}_1$ is the result of two contributions, i.e. $\boldsymbol{u}_g$ containing the shaker excitations, and $\boldsymbol{n}_g$ containing the environmental floor vibrations. The shaker block represents the transfer function from reference $\boldsymbol{r}$ to $\boldsymbol{u}_g$, with $\boldsymbol{r}$ being the output of a pseudo-random noise signal generator. The output signal $\boldsymbol{y}_1$ consists of $\boldsymbol{y}_p$ representing payload motion caused by BF vibrations, and process noise $\boldsymbol{n}_p$ representing payload motion due to direct payload disturbances (e.g., acoustic waves). Measurements of $\boldsymbol{u}_1$ and $\boldsymbol{y}_1$ are filtered with band-pass filters, which are assumed to behave as an ideal band-pass filter, see Assumption 1. Moreover, the measured signals contain additive measurement noise $\boldsymbol{m}_u$ and $\boldsymbol{m}_y$, respectively. After sampling, the BF and payload measurements are converted to Cartesian coordinates using the blocks $\mathbf{T_u}$ and $\mathbf{T_y}$, respectively, which results in the signals $\boldsymbol{u}$ and $\boldsymbol{y}$. These signals represent sampled-data signals $\boldsymbol{u}(nT_s), \boldsymbol{y}(nT_s)$ having sampling time T_s and $n \in \{0, 1, \ldots, N-1\}$.

Assumption 1 (*Ideal band-pass filter*). An ideal band-pass filter with a frequency band ranging from $\omega_{\text{BP, min}}$ to $\omega_{\text{BP, max}}$ produces a band-limited output signal $u_{BP}(t)$ of input signal $u(t)$, i.e. $U_{BP}(\omega) = U(\omega)$ for $\omega_{\text{BP, min}} < |\omega| < \omega_{\text{BP, max}}$, and $U_{BP}(\omega) = 0$ for all other frequencies ω.

4.1. Spectral analysis

To identify MIMO systems using random excitations and spectral analysis, a full record of data $\boldsymbol{y}, \boldsymbol{u}$ is measured for a sufficiently long time. Subsequently, the full record is split into M possibly overlapping subrecords of equal length denoted $\boldsymbol{y}^{[l]}, \boldsymbol{u}^{[l]}$, with $l \in \{1, \ldots, M\}$. These subrecords are multiplied with a Hanning window $w(nT_s)$ to reduce the effects of leakage [15, Section 2.6]. Then, the discrete Fourier transforms (DFT) $\boldsymbol{Y}^{[l]}(\omega)$ and $\boldsymbol{U}^{[l]}(\omega)$ of the windowed signals are defined as

$$\boldsymbol{U}^{[l]}(\omega_k) = \frac{1}{S_2} \sum_{n=0}^{N-1} w(nT_s) \boldsymbol{u}^{[l]}(nT_s) e^{-j\omega_k nT_s}, \tag{3}$$

$$\boldsymbol{Y}^{[l]}(\omega_k) = \frac{1}{S_2} \sum_{n=0}^{N-1} w(nT_s) \boldsymbol{y}^{[l]}(nT_s) e^{-j\omega_k nT_s}, \tag{4}$$

where only the N frequencies $\omega_k = (2\pi k)/(NT_s), k \in \{0, \ldots, N-1\}$ are considered. In view of Assumption 1, it is assumed that $\omega_{\text{BP, min}} < \omega_k < \omega_{\text{BP, max}}$ for all k. In the remainder of this paper, the abuse of notation $\omega \equiv \omega_k$ is used with the intention to improve readability. The scaling factor

$$S_2 = \sqrt{\sum_{n=0}^{N-1} |w(nT_s)|^2}, \tag{5}$$

is chosen such that the transformation preserves the root mean square (RMS) value of the signal [15, Section 7.2].

Having calculated all $\boldsymbol{Y}^{[l]}(\omega)$ and $\boldsymbol{U}^{[l]}(\omega)$, estimates for the cross power spectral density (PSD) matrix $\widehat{\mathbf{S}}_{\mathbf{YU}}(\omega)$ and auto PSD matrix $\widehat{\mathbf{S}}_{\mathbf{UU}}(\omega)$ are obtained by averaging over the M blocks, i.e.

$$\widehat{\mathbf{S}}_{\mathbf{YU}}(\omega) = \left(\frac{2}{f_s}\right) \frac{1}{M} \sum_{l=1}^{M} \boldsymbol{Y}^{[l]}(\omega) (\boldsymbol{U}^{[l]}(\omega))^H, \tag{6}$$

$$\widehat{\mathbf{S}}_{\mathbf{UU}}(\omega) = \left(\frac{2}{f_s}\right) \frac{1}{M} \sum_{l=1}^{M} \boldsymbol{U}^{[l]}(\omega) (\boldsymbol{U}^{[l]}(\omega))^H. \tag{7}$$

In (6) and (7), a scaling factor $2/f_s$ is included to obtain a single-sided PSD matrix with the physical unit $(\text{m/s}^2)^2/\text{Hz}$ [31]. Neglecting the effects of leakage and windowing, and under the assumption of perfect anti-aliasing provided by the band-pass filters, an estimate for $\mathcal{T}$ is obtained using the so-called H_1 estimator, see, e.g. [15,32],
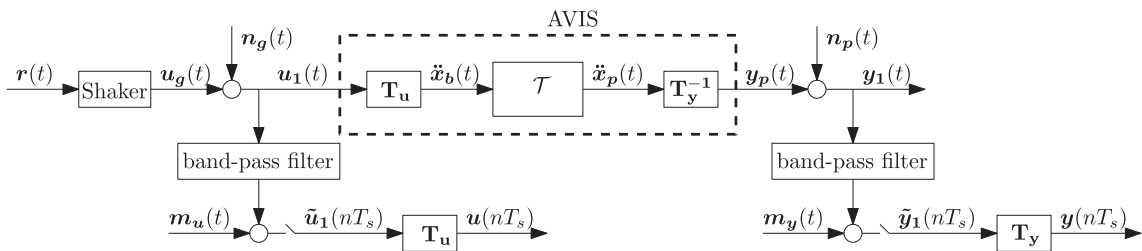
Fig. 2. Block diagram for non-parametric system identification via measurements. Base frame motion is measured by $\boldsymbol{u}_1$, payload motion by $\boldsymbol{y}_1$. Band-pass filters are applied in the signal conditioners to prevent aliasing and to suppress sensor noise. The transformed signals $\boldsymbol{u}, \boldsymbol{y}$ represent base frame and payload motion, respectively, expressed in the same Cartesian coordinate frame, see (1).

$$\hat{T}(j\omega) = \widehat{\mathbf{S}}_{\mathbf{YU}}(\omega)\widehat{\mathbf{S}}_{\mathbf{UU}}^{-1}(\omega). \tag{8}$$

The H_1 estimator is a suitable choice when the input SNR of $\boldsymbol{u}$ is much better than the output SNR of $\boldsymbol{y}$. Contrarily, when the output SNR is much better than the input SNR, the H_2 estimator is preferred [19]. When the input and output SNR are similar, and there is a priori knowledge about the noise spectra, more advanced estimators can be defined that result in reduced bias, see, e.g., [33,34]. However, in the context of vibration isolation, the SNR of $\boldsymbol{u}$ is typically much higher than the SNR of $\boldsymbol{y}$, at least beyond the suspension frequency where isolation occurs. Therefore, the H_1 estimator typically gives the best estimates.

4.2. Bias, variance, and the 95% confidence regions

This section presents expressions for bias and variance of the H_1 estimator in (8), where the variance can be used to construct the 95% confidence region which is defined below. To this end, the inputs and outputs are written in the frequency domain as

$$\begin{aligned}\boldsymbol{U}(\omega) &= \boldsymbol{U_0}(\omega) + \boldsymbol{N_U}(\omega),\\ \boldsymbol{Y}(\omega) &= \boldsymbol{Y_0}(\omega) + \boldsymbol{N_Y}(\omega),\end{aligned} \tag{9}$$

with corresponding noise-free input and output

$$\begin{aligned}\boldsymbol{U_0}(\omega) &= \mathbf{T_u}(\boldsymbol{U_G}(\omega) + \boldsymbol{N_G}(\omega)),\\ \boldsymbol{Y_0}(\omega) &= \mathcal{T}(j\omega)\boldsymbol{U_0}(\omega),\end{aligned} \tag{10}$$

and input and output noise

$$\begin{aligned}\boldsymbol{N_U}(\omega) &= \mathbf{T_u}\boldsymbol{M_U}(\omega),\\ \boldsymbol{N_Y}(\omega) &= \mathbf{T_y}(\boldsymbol{N_P}(\omega) + \boldsymbol{M_Y}(\omega)).\end{aligned} \tag{11}$$

In these equations, $\boldsymbol{U_G}, \boldsymbol{N_G}, \boldsymbol{N_P}, \boldsymbol{M_U}, \boldsymbol{M_Y}$ represent frequency-domain representations of the time-domain signals $\boldsymbol{u_g}, \boldsymbol{n_g}, \boldsymbol{n_p}, \boldsymbol{m_u}, \boldsymbol{m_y}$ indicated in Fig. 2.

The following assumptions are introduced regarding the noise, and are consistent with [15, Section 16.16]:

Assumption 2 (*Noise disturbance*). The DFTs $\boldsymbol{N_U}(\omega), \boldsymbol{N_Y}(\omega)$ of the noise signals in (11) are circular complex normally distributed. This leads to the following properties:

$$\begin{aligned}&\mathbb{E}[\boldsymbol{N_U}(\omega)] = \boldsymbol{0}, \quad \mathbb{E}[\boldsymbol{N_Y}(\omega)] = \boldsymbol{0},\\ &\mathbb{E}\Big[\boldsymbol{N_U}(\omega)\boldsymbol{N_U}^T(\omega)\Big] = \boldsymbol{0}, \quad \mathbb{E}\Big[\boldsymbol{N_Y}(\omega)\boldsymbol{N_Y}^T(\omega)\Big] = \boldsymbol{0}, \quad \mathbb{E}\Big[\boldsymbol{N_Y}(\omega)\boldsymbol{N_U}^T(\omega)\Big] = \boldsymbol{0},\\ &\mathbb{E}\Big[\boldsymbol{N_U}(\omega)\boldsymbol{N_U}^H(\omega)\Big] = \mathbf{C_U}(\omega), \quad \mathbb{E}\Big[\boldsymbol{N_Y}(\omega)\boldsymbol{N_Y}^H(\omega)\Big] = \mathbf{C_Y}(\omega), \quad \mathbb{E}\Big[\boldsymbol{N_Y}(\omega)\boldsymbol{N_U}^H(\omega)\Big] = \mathbf{C_{YU}}(\omega).\end{aligned} \tag{12}$$

Assumption 3 (*Noise disturbance – continued*). The noise signals $\boldsymbol{N_U}, \boldsymbol{N_Y}$ in (11) are independent of the signals $\boldsymbol{U_0}, \boldsymbol{Y_0}$ in (10).

Under Assumptions 2 and 3, and under the assumption that there is no input noise, i.e. $\mathbf{C_U} = \mathbf{C_{YU}} = \boldsymbol{0}$, it is shown in [15] that the H_1 estimator (8) is unbiased. The latter assumption holds if $\boldsymbol{U}$ is measured with a sufficiently large SNR, which is discussed further in Section 5. Under the same assumptions, $\hat{T}$ is asymptotically circular complex normally distributed where an estimation for the covariance matrix of $\hat{T}$ is given by [15, Section 7.2.3]

$$\text{Cov}(\text{vec}(\hat{T}(j\omega))) = \frac{1}{M}\Big(\widehat{\mathbf{S}}_{\mathbf{UU}}^{-1}(\omega)\Big)^T \otimes \widehat{\mathbf{C}}_{\mathbf{Y}}(\omega), \tag{13}$$

where the output noise covariance is estimated as

$$\widehat{\mathbf{C}}_{\mathbf{Y}}(\omega) = \frac{M}{q}\Big(\widehat{\mathbf{S}}_{\mathbf{YY}}(\omega) - \widehat{\mathbf{S}}_{\mathbf{YU}}(\omega)\widehat{\mathbf{S}}_{\mathbf{UU}}^{-1}(\omega)\widehat{\mathbf{S}}_{\mathbf{YU}}^H(\omega)\Big), \tag{14}$$

with $q = M - n_u$ the number of degrees of freedom in the residual [15]. Eq. (13) results in an $(n_y n_u) \times (n_y n_u)$ matrix. The entries on the main diagonal of this matrix represent estimations of the squared standard deviations $\hat{\sigma}^2(\hat{T}_{i,j})$ for all entries $[i,j]$ of $\hat{T}$, with $i \in \{1,\ldots,n_y\}; j \in \{1,\ldots,n_u\}$. Subsequently, the most compact 95% confidence region for each entry $[i,j]$ of $\hat{T}$ is defined as a circle with radius $\sqrt{3}\hat{\sigma}(\hat{T}_{i,j})$ [15, Section 7.2.4]. This region is used to indicate the uncertainty due to output noise in the measurements presented in Section 6.

Note that the previous conditions regarding bias and the 95% confidence region assume that $\mathbf{C_U} = \mathbf{C_{YU}} = \boldsymbol{0}$. Moreover, the H_1 estimator assumes that $\widehat{\mathbf{S}}_{\mathbf{UU}}$ is invertible, i.e. there is sufficient uncorrelated spectral power in all input directions. However, these assumptions are violated when one or more input directions are strongly correlated or have a poor SNR due to insufficient spectral power. As a consequence, the estimated FRF and the 95% confidence regions might become inaccurate. To assess the quality of $\widehat{\mathbf{S}}_{\mathbf{UU}}$, an input excitation analysis and design method is presented in Section 5.

Remark 4. In (8), the *direct* estimation method has been applied [15], i.e. the estimation of $\mathcal{T}$ is based on measurement data of $\boldsymbol{u}$ and $\boldsymbol{y}$ only. An alternative is to use the *indirect* method [15], which also uses data of the user-defined shaker forces $\boldsymbol{r}$ and therefore can provide unbiased estimates for $\mathcal{T}$ even if there is a significant contribution of (input) noise. However, the drawback of indirect methods is that $\boldsymbol{n_g}$, which includes useful environmental floor excitations, cannot be used for identification. Therefore, indirect methods are not useful in view of the considered problem in this paper.

5. Input excitation analysis and design

In order to accurately estimate $\mathcal{T}$, the input excitations of the base frame must satisfy two requirements. First, $\widehat{\mathbf{S}}_{\mathbf{UU}}$ must be invertible, and second, the 95% confidence regions must be sufficiently small. These requirements are generally not satisfied in experiments with only environmental vibrations. In that case, BF vibrations can be augmented with shaker excitations. Proper design of the shaker input signals is essential to achieve sufficient BF excitation while minimizing the experiment cost. This design problem is known in literature as optimal input design [16]. This section presents two steps towards such an input design method. In the first step, requirements for the spectral input power are derived to accurately estimate $\mathcal{T}$. In the second step, Cartesian input directions are detected that need shaker excitations to fulfill the requirements with minimum experiment cost.

Remark 5. Many examples can be found in literature to optimize the input signal such that a parametric model can be fitted with a sufficiently low variance, see, e.g., [16] and the references therein. In this paper, however, the main objective is to find an input signal to minimize the bias and variance of an estimated non-parametric model (FRF). Since the frequency data points are independent, input design will be performed by optimizing the SNR at all frequency points of interest. Afterwards, optimal time-domain signals for shaker excitations can be generated, see, e.g., [16,35].

5.1. Requirements on spectral input power

Requirements on spectral input power should be such that $\widehat{\mathbf{S}}_{\mathbf{UU}}$ is invertible and the 95% confidence regions are sufficiently small, see Section 4.2. In the following, it will be shown that these two requirements can be assessed via principal component analysis [33,36], which evaluates the uncorrelated input excitations. For this analysis method, the original sensor signals $\widetilde{\boldsymbol{U_1}}$ are used rather than the transformed Cartesian coordinates $\boldsymbol{U}$ for two reasons. First, it ensures that all sensor units are the same, i.e. m/s², to prevent unit scaling problems. Second, it preserves a specific structure of the noise covariance matrix, which will be further explained in Section 5.1.1. This structure would otherwise have been lost by multiplication of the signals with transformation matrix $\mathbf{T_u}$. First, principal component analysis will be presented, and, second, conditions are derived to satisfy the requirements.

5.1.1. Principal component analysis

The principal components are calculated by the eigenvalue decomposition (EVD) of $\widehat{\mathbf{S}}_{\widetilde{\mathbf{U_1}}\widetilde{\mathbf{U_1}}}$, which is the PSD matrix of $\widetilde{\boldsymbol{U_1}}$ and which is defined similar to (7). By definition, $\widehat{\mathbf{S}}_{\widetilde{\mathbf{U_1}}\widetilde{\mathbf{U_1}}}$ is a Hermitian matrix ($\mathbf{A} = \mathbf{A}^H$) which has an EVD

$$\widehat{\mathbf{S}}_{\widetilde{\mathbf{U_1}}\widetilde{\mathbf{U_1}}}(\omega) = \widetilde{\mathbf{T}}_{\mathbf{Q}}(\omega)\tilde{\mathbf{\Lambda}}(\omega)\widetilde{\mathbf{T}}_{\mathbf{Q}}^H(\omega). \tag{15}$$

In (15), $\tilde{\mathbf{\Lambda}}(\omega) = \mathrm{diag}(\tilde{\lambda}_1(\omega), \ldots, \tilde{\lambda}_n(\omega))$ contains the eigenvalues of $\widehat{\mathbf{S}}_{\widetilde{\mathbf{U_1}}\widetilde{\mathbf{U_1}}}(\omega)$ that represent spectral powers of the principal components, and the columns of the $n_u \times n_u$ unitary matrix $\widetilde{\mathbf{T}}_{\mathbf{Q}}(\omega)$ contain the normalized eigenvectors that indicate the directions of the principal components. Matrix $\widetilde{\mathbf{T}}_{\mathbf{Q}}$ can be used to transform the noisy sensor signals $\widetilde{\boldsymbol{U_1}}$ to the noisy principal coordinates $\widetilde{\boldsymbol{Q}}$ via

$$\widetilde{\boldsymbol{Q}}(\omega) = \widetilde{\mathbf{T}}_{\mathbf{Q}}^H(\omega)\widetilde{\boldsymbol{U_1}}(\omega) = \widetilde{\mathbf{T}}_{\mathbf{Q}}^H(\omega)\boldsymbol{U_1}(\omega) + \widetilde{\mathbf{T}}_{\mathbf{Q}}^H(\omega)\boldsymbol{M_U}(\omega), \tag{16}$$

with noise-free excitation signal $\boldsymbol{U_1}$ and noise $\boldsymbol{M_U}$ as defined in Fig. 2. The noise term $\widetilde{\mathbf{T}}_{\mathbf{Q}}^H\boldsymbol{M_U}$ contributes to $\widetilde{\boldsymbol{Q}}$, which can lead to bias in the estimated power and directions of the principal components. To deal with this problem, the following assumption is introduced regarding the noise.

Assumption 6. The noise signals in $\boldsymbol{M_U}(\omega)$ are uncorrelated, have zero mean, and variance $\sigma_{\mathrm{acc}}^2(\omega)$ such that $\boldsymbol{U_1}(\omega)$ has noise covariance matrix $\mathbf{C}_{\boldsymbol{U_1}\boldsymbol{U_1}}(\omega) = \sigma_{\mathrm{acc}}^2(\omega)\mathbf{I}_{n_u}$.

Assumption 6, which has also been used in [36], can be motivated from the fact that accelerometers of the same type are used to measure $\boldsymbol{U_1}$. Therefore, it is reasonable to assume that all accelerometers have uncorrelated measurement noise with similar standard deviation. Under Assumptions 3 and 6, and for the number of averages $M \to \infty$, the eigenvectors of the prin-

cipal components derived from the noisy measurements $\widetilde{\boldsymbol{U_1}}$ asymptotically converge to the eigenvectors of the principal components that would be obtained from a noise-free measurement of $\boldsymbol{U_1}$. Under the same conditions, each principal component is measured with signal-to-noise ratio

$$(SNR)_i(\omega) = \frac{\tilde{\lambda}_i(\omega)}{\sigma^2_{acc,u}(\omega)}, \quad i \in \{1, \ldots, n_u\}. \tag{17}$$

(see Appendix B) with $\tilde{\lambda}_i$ the diagonal elements from $\tilde{\boldsymbol{\Lambda}}$ in (15).

5.1.2. Conditions for input SNR

The result in (17) can be used to check if the input excitations in $\boldsymbol{u_1}$ are sufficiently powerful and uncorrelated such that the input spectrum is invertible. To ensure this, all principal components should have sufficient SNR, or

$$\tilde{\lambda}_i(\widehat{\boldsymbol{S}}_{\widetilde{\boldsymbol{U_1}}\widetilde{\boldsymbol{U_1}}}(\omega)) > (SNR_{min})\sigma^2_{acc,u}(\omega), \quad \forall i, \tag{18}$$

with (SNR_{min}) the user-defined minimum SNR.

Given that the input spectrum is invertible, identification of $\mathcal{T}(j\omega)$ with a low variance and a small 95% confidence region is desired. To this end, conditions regarding the variance are translated to conditions on the spectral input power in Appendix C. The resulting condition is given by

$$\tilde{\lambda}_i\left(\widehat{\boldsymbol{S}}_{\widetilde{\boldsymbol{U_1}}\widetilde{\boldsymbol{U_1}}}(\omega)\right) > \frac{1}{M}\frac{\sigma^2_{acc,y}(\omega)}{(VAR_{max})\varsigma^2(\omega)}, \quad \forall i. \tag{19}$$

with M the number of averaged windows, and $\sigma^2_{acc,y}$ the sensor noise level of the payload accelerometers. $(VAR_{max}) \in \mathbb{R}$ is user-defined and gives the allowed variance relative to ς which is the lowest singular value of $\mathcal{T}_l = \boldsymbol{T_y}^{-1}\mathcal{T}\boldsymbol{T_u}$ representing the transmissibility matrix in local sensor coordinates, i.e. from $\boldsymbol{U_1}$ to $\boldsymbol{Y_1}$.

Conditions (18) and (19) can be replaced by the single condition

$$\tilde{\lambda}_i(\widehat{\boldsymbol{S}}_{\widetilde{\boldsymbol{U_1}}\widetilde{\boldsymbol{U_1}}}(\omega)) > \max\left((SNR_{min})\ \sigma^2_{acc,u}(\omega), \frac{1}{M}\frac{\sigma^2_{acc,y}(\omega)}{(VAR_{max})\varsigma^2(\omega)}\right), \quad \forall i. \tag{20}$$

If (20) is not satisfied for all i, the BF excitation power needs to be increased using shakers. In view of minimizing experiment cost, only the power of insufficiently excited directions should be increased. This requires knowledge about the weakest excited directions. This information can be obtained from a method that calculates the so-called projection similarity, which is explained in Section 5.2.

5.2. Projection similarity

This section proposes the projection similarity, which is a performance measure that can be used to discriminate between the input directions with sufficient and insufficient excitation power. This information can subsequently be used for input design of the shaker signals. To determine the projection similarity, first the set of vectors $\{\boldsymbol{x}_1, \ldots, \boldsymbol{x}_{n_u}\}$ representing the Cartesian components expressed in sensor coordinates is defined:

$$\boldsymbol{T_u}^{-1} = [\boldsymbol{x}_1(\omega) \quad \boldsymbol{x}_2(\omega) \quad \ldots \quad \boldsymbol{x}_{n_u}(\omega)]. \tag{21}$$

When the vectors with Cartesian components are normalized, one obtains

$$\bar{\boldsymbol{x}}_i(\omega) = \frac{1}{\|\boldsymbol{x}_i\|_2}\boldsymbol{x}_i, \quad i \in \{1, \ldots, n_u\}, \tag{22}$$

with $\|\ldots\|_2$ representing the 2-norm. A second set of eigenvectors $\{\boldsymbol{q}_1, \ldots, \boldsymbol{q}_{n_u}\}$ corresponding to the principal components expressed in sensor coordinates is defined as

$$\boldsymbol{T_Q}(\omega) = \begin{bmatrix} \boldsymbol{q}_1(\omega) & \boldsymbol{q}_2(\omega) & \ldots & \boldsymbol{q}_{n_u}(\omega) \end{bmatrix}. \tag{23}$$

Next, the normalized Cartesian components $\bar{\boldsymbol{x}}_i$ are written as a linear combination of the principal components $\boldsymbol{q}_i$:

$$\bar{\boldsymbol{x}}_i(\omega) = c_1(\omega)\boldsymbol{q}_1(\omega) + \cdots + c_{n_u}(\omega)\boldsymbol{q}_{n_u}(\omega), \quad \text{with} \quad \begin{bmatrix} c_1(\omega) \\ \vdots \\ c_{n_u}(\omega) \end{bmatrix} = \boldsymbol{T_Q}^{-1}(\omega)\bar{\boldsymbol{x}}_i(\omega), \quad i \in \{1, \ldots, n_u\}. \tag{24}$$

Now suppose that only the first m principal components have sufficient spectral power. Then, (24) can be written as

$$\bar{\boldsymbol{x}}_i(\omega) = \underbrace{c_1(\omega)\boldsymbol{q}_1(\omega) + \cdots + c_m(\omega)\boldsymbol{q}_m(\omega)}_{\hat{\bar{\boldsymbol{x}}}_i(\omega)} + \underbrace{c_{m+1}(\omega)\boldsymbol{q}_{m+1}(\omega) + \ldots + c_{n_u}(\omega)\boldsymbol{q}_{n_u}(\omega)}_{\bar{\boldsymbol{x}}_i^\perp(\omega)}, \quad i \in \{1, \ldots, n_u\}. \tag{25}$$

In (25), $\hat{\bar{\boldsymbol{x}}}_i$ represents the orthonormal projection of $\bar{\boldsymbol{x}}_i$ in the subspace spanned by the sufficiently excited principal components $\{\boldsymbol{q}_1, \ldots, \boldsymbol{q}_m\}$. This is because the vectors $\boldsymbol{q}_i$ form an orthonormal basis for $\{\boldsymbol{q}_1, \ldots, \boldsymbol{q}_{n_u}\}$ since $\mathbf{T}_\mathbf{Q}$ is a unitary matrix by definition of (15). Define $(PE)_i \in [0, 1]$ as the projection error of the ith Cartesian component, i.e.,

$$(PE)_i(\omega) = \|\bar{\boldsymbol{x}}_i(\omega) - \hat{\bar{\boldsymbol{x}}}_i(\omega)\|_2, \quad i \in \{1, \ldots, n_u\}. \tag{26}$$

The maximum projection error equals 1, because the length of $\bar{\boldsymbol{x}}_i$ is 1. From $(PE)_i$, the projection similarity in the ith Cartesian component $(PS)_i \in [0, 1]$ is defined as

$$(PS)_i(\omega) = 1 - (PE)_i(\omega), \quad i \in \{1, \ldots, n_u\}. \tag{27}$$

The projection similarity (PS) gives information about the ability to express a Cartesian component as a linear combination of the sufficiently excited principal components. On the one hand, a high PS means a large spectral power in that Cartesian component of the BF excitation. On the other hand, a low PS means that there will be little spectral power in that Cartesian component, and shakers should be used to increase the power. As such, the PS provides a tool for input design of the shaker signals, which is demonstrated during the experimental validation in the next section.

6. Experimental results

The results of two identification experiments are presented in this section to show the viability of the proposed approach to deal with heavy-weight systems. In the first experiment, the shakers are switched off such that the BF is only excited by environmental floor vibrations. The results of this experiment are used to gain insight in the spectral input power and directions of the environmental excitations. Based on these results, the shaker excitation signals are designed such that the BF excitation power is sufficiently increased for all frequencies and in all directions.

The shaker experiment design step is described in Section 6.1. The resulting FRF estimates for the transmissibility matrix $\mathcal{T}$ from both experiments are presented and validated with the parametric model in Section 6.2. For both experiments, a 10-min long measurement sequence of $\boldsymbol{u}$ and $\boldsymbol{y}$ is conducted, which is split up into 60 sub-records of 10 s each. Each sub-record is filtered using a Hanning window. To compensate for data loss due to windowing, a 50% overlap factor is used resulting in averaging over $M = 119$ subrecords. For clarity of presentation, only the directions (z, θ_x, θ_y) are considered, but the results directly apply to the directions (x, y, θ_z).

6.1. Experiment design: shaker signals

As explained in Section 5, the input spectral power should be such that $\hat{\mathbf{S}}_{\mathbf{UU}}$ is invertible and that the 95% confidence region is sufficiently small. These requirements are validated by considering the SNR condition in (20). To this end, consider the plot in Fig. 3a representing the spectral powers of the principal components of $\hat{\mathbf{S}}_{\tilde{\mathbf{U}}_1 \tilde{\mathbf{U}}_1}$. For the experiment without shaker excitation it is observed that only one principal power is above the line of minimum power in the frequency region from 2 to 15 Hz. The minimum power is defined according to (20) with $(SNR_{min}) = 30$, such that the SNR is sufficiently above the ADC noise floor of $3.3 \cdot 10^{-12} \ (\text{m/s}^2)^2/\text{Hz}$, and the relative variance $(VAR_{max}) = 0.1$ such that the 95% confidence region is sufficiently small. The local transmissibility matrix is estimated as $\mathcal{T}_l = \mathbf{T}_\mathbf{y}^{-1} \mathcal{T} \mathbf{T}_\mathbf{u}$ using the parametric model for $\mathcal{T}$ in (A.6). When
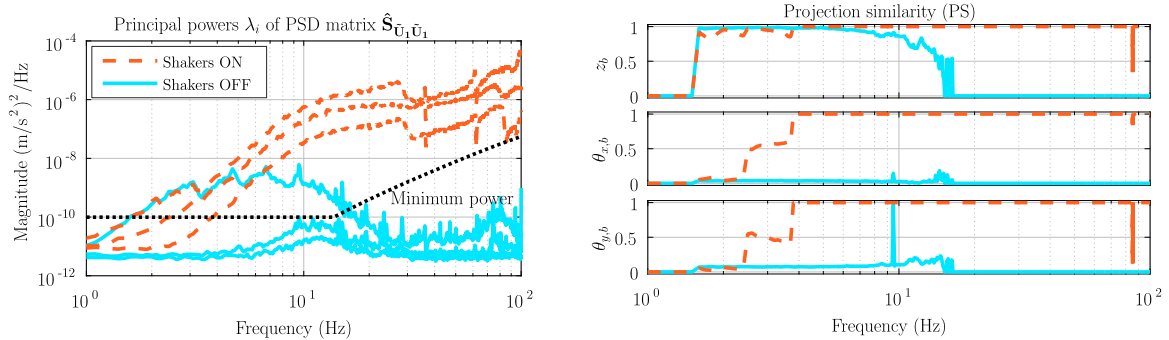
(a) Principal powers of the auto-power spectrum matrix $\hat{\mathbf{S}}_{\tilde{\mathbf{U}}_1 \tilde{\mathbf{U}}_1}$ for both experiments. The black dotted line represents the minimum spectral power defined by (20) with $SNR_{min} = 30$ and $VAR_{max} = 0.1$.

(b) Projection similarity (PS) plot, see (27). The legend for this figure is omitted, since it is identical to the legend in Figure 3a.

Fig. 3. Analysis of the BF excitation for both experiments. The experiment without shaker excitation shows insufficient power in multiple frequency regions and directions. By enabling the shakers, sufficient power is obtained for almost all frequencies.

analyzing the projection similarity (PS) plot in Fig. 3b, it is observed that for frequencies between 2 and 15 Hz the floor is mainly exciting the BF in the z-direction, while there is almost no excitation in the θ_x- and θ_y-directions. Outside this frequency region, the excitation level is clearly insufficient in all directions.

For the second experiment, shakers are used to increase the spectral input power. Since Fig. 3b shows that the floor is not providing sufficient power in any of the three Cartesian components beyond 15 Hz, three shakers are enabled simultaneously to increase the spectral power in all three directions. The input signals for the shakers consist of three uncorrelated white noise signals, which are filtered such that all principal powers are exceeding the minimum required power at most frequencies. Using the shakers, Fig. 3a shows that the spectral power of all principal components is greatly increased. For frequencies below 10 Hz it is difficult to largely increase the BF excitation level due to the mechanical limits of the shakers, but the figure shows that for frequencies beyond 4 Hz (almost) all directions now have a sufficient SNR. The figure also shows the benefit of combining the spectral power from the floor and the shakers. The spectral power from the floor drops for frequencies beyond 10 Hz, while the shakers are not able to dominate all principal components of the floor for frequencies below 7 Hz. Considering Fig. 3b, it is observed that all three Cartesian coordinates now have a PS of 1, hence sufficient excitation, for frequencies beyond 4 Hz. At low frequencies there is still insufficient excitation, in particular in the θ_x- and θ_y directions, to provide a reliable estimate. For these frequencies and directions, the parametric model can be used to estimate $\mathcal{T}$.

6.2. Transmissibility matrix measurements

Bode plots are presented for both experiments to show $\widehat{\mathcal{T}}$ as defined in (8), and the most compact 95% confidence region as defined in Section 4.2. The measurement results are compared with the parametric model presented in Section 2.2 to validate the measurements.

6.2.1. Experiment with only floor excitations

Fig. 4 shows measurement results for $\hat{\mathcal{T}}$ in the first experiment where the shakers are disabled. Below 20 Hz, only the subplots having z_b as input are trusted because the floor is mainly exciting the BF in this direction, recall Fig. 3b. Only in these parts of Fig. 4 the confidence regions are sufficiently small, and the measured FRF generally coincides with the parametric model. The latter indicates that the parametric model is sufficiently accurate at the lower frequencies. The measured FRFs also show the roll-off as predicted by the model up to 20 Hz, clearly showing the benefit of vibration isolation. Moreover,
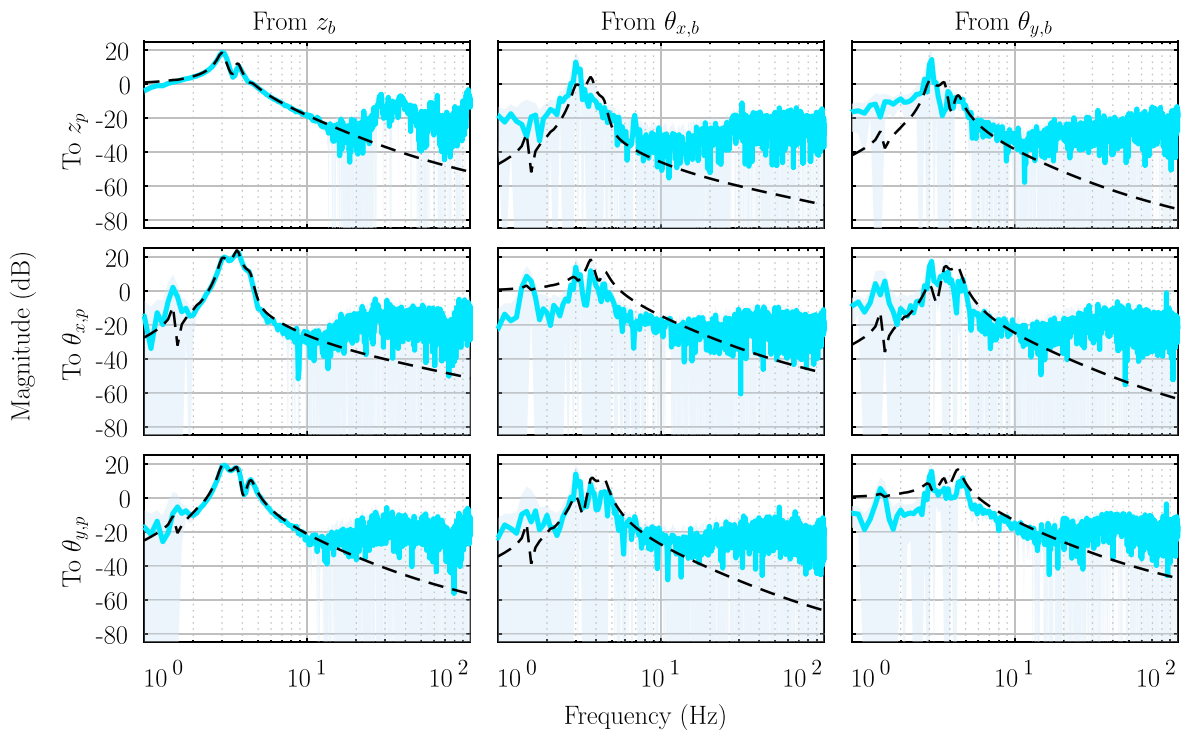
Fig. 4. Bode magnitude plot showing the transmissibility matrix $\hat{\mathcal{T}}$ for the first experiment with only floor excitations. The solid blue lines represents $\hat{\mathcal{T}}$, while the shaded areas represent the 95% confidence regions as defined in Section 4.2. The dashed black lines correspond to the modeled transmissibility matrix, see (A.6). In this experiment, $\hat{\mathcal{T}}$ is only accurate in the z_b input directions between 2–10 Hz because only this region has sufficient excitation power, see Fig. 3. (For interpretation of the references to colour in this figure legend, the reader is referred to the web version of this article.)

all three subplots have a desired small confidence region between 2 and 10 Hz, indicating sufficient output SNR. Beyond 15 Hz, the roll-off in $\hat{\mathcal{T}}$ stops, but here the requirements regarding the input are not satisfied (see Fig. 3b), which leads to a large uncertainty (see Fig. 4), hence an unreliable FRF estimate.

In general, the FRF measurements for this experiment should be taken with care because $\hat{\mathbf{S}}_{UU}$ is ill-conditioned. Although the projection similarity for z_b is close to 1 for frequencies 2–15 Hz, the FRF could be heavily biased due to cross-coupling in the transmissibility matrix. In that case, a small perturbation of a discarded principal component in (25) might still give a large difference in the output responses, leading to inaccurate FRF estimates.

6.2.2. Experiment with floor and shaker excitations

Fig. 5 shows measurement results for $\hat{\mathcal{T}}$ in the second experiment with enabled shaker excitations. Along the plots, three vertical suspension modes appear around 3–5 Hz. At 1.5 Hz, a horizontal suspension mode appears due to cross-coupling in $\mathcal{T}$ and non-perfect alignment of the setup. Below 4 Hz, significant discrepancies are visible between the model and the measurement. In this region, the model should be correct because below the suspension modes the main diagonal of the transmissibility matrix should have 0 dB magnitude while the off-diagonal terms tend to zero for lower frequencies, see Remark 7 in Appendix A. The incorrect measurement at low frequencies is mainly due to an insufficient input SNR, see Fig. 3b. For the mid- and higher frequencies, Fig. 5 shows a good agreement between the measurement and the parametric model. Compared to Fig. 4 of the first experiment, Fig. 5 shows better roll-off beyond 15 Hz in all directions, as predicted from the parametric model. The 95% confidence regions are very small, indicating a sufficient output SNR and a reliable FRF estimate. At the higher frequencies, some (anti-) resonance peaks appear due to flexibilities in the BF. In fact, beyond the first resonance frequency around 27 Hz. Then, the BF can no longer be considered as a rigid body, such that four accelerometers at the BF are necessary to uniquely measure $\mathcal{T}$. Note that the accelerometers are not perfectly aligned with the air mounts which can induce the visibility of structural dynamics of the BF, recall Section 2.2. In addition, the first resonance frequency of the payload occurs at 121 Hz, which is also responsible for the occurrence of anti-resonances at the lower frequencies.

Another potential cause of additional anti-(resonances) and bias showing up is found in the fact that horizontal BF excitations are neglected. However, the shakers also induce parasitic horizontal motion at the isolator locations because the shakers are not perfectly aligned with the isolators. Since the validation was only concerned with estimations in the directions (z, θ_x, θ_y), vertical payload motion due to horizontal BF excitation and mechanical cross-coupling in the transmissibility matrix shows up as output noise $\boldsymbol{n_p}$, which is correlated with the vertical BF excitations. As such, Assumption 2 for
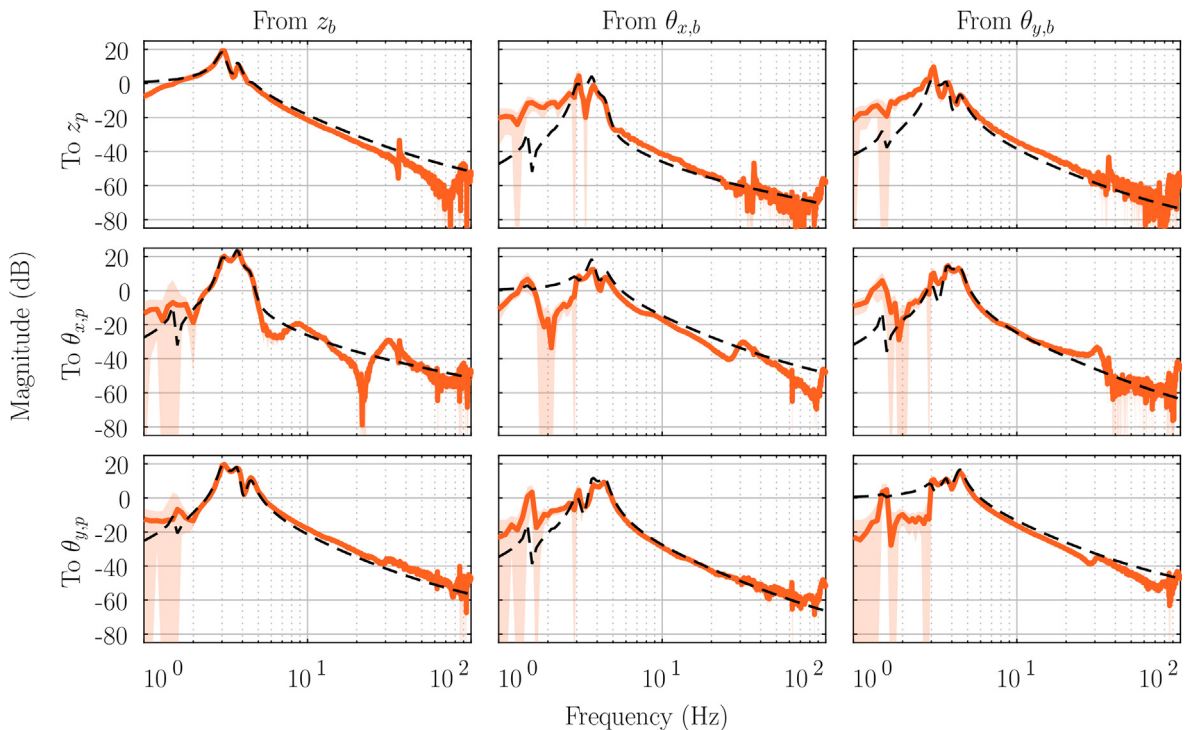
Fig. 5. Bode magnitude plot showing the transmissibility matrix for the second experiment with both floor and shaker excitations. The solid red lines represent $\hat{\mathcal{T}}$, while the shaded areas represent the 95% confidence regions as defined in Section 4.2. The dashed black lines correspond to the modeled transmissibility matrix, see (A.6). Compared to Fig. 4, $\hat{\mathcal{T}}$ is now accurately estimated for most frequencies and input directions due to increased excitation power, see Fig. 3. (For interpretation of the references to colour in this figure legend, the reader is referred to the web version of this article.)

uncorrelated output noise no longer holds, which leads to bias in $\hat{\mathcal{T}}$. However, since both the parasitic horizontal excitation and the horizontal-to-vertical cross-coupling are expected to be sufficiently small with respect to the vertical excitation and the vertical-to-vertical coupling in the transmissibility matrix, it is generally considered fair to neglect this parasitic effect.

7. Conclusions

A non-parametric identification approach based on spectral analysis is presented to estimate the transmissibility matrix of an industrial active vibration isolation system. Measurements without shaker excitation can only provide a good FRF estimate for the outputs related to the z_b input direction, because floor vibrations mainly occur in this input direction. This follows from the developed analysis method based on principal component analysis. Measurements with enabled shaker excitation can provide reliable measurements for frequencies from 4 to 100 Hz in three directions. This result is obtained by proper input design of the shaker signals as described in this paper. For lower frequencies, the shakers are unable to sufficiently excite the BF. The measurements are validated using a parametric model for the transmissibility matrix, which can be derived from the compliance function that is accurately identified. This validation generally shows a good fit of the measurement with the parametric model, and completes the transmissibility matrix estimation as a whole.

Acknowledgment

Appendix A. Derivation of the parametric model

A parametric model of the transmissibility matrix can be derived indirectly from the so-called compliance matrix $\mathcal{C}$. The latter represents the transfer function matrix from payload forces $\boldsymbol{f}_l$ to payload motion $\boldsymbol{x_p}$, see Fig. A.6. Since the AVIS considered in Section 2 is a so-called *active* vibration isolation system, each isolator contains a horizontal and a vertical Lorentz actuator intended for active vibration isolation and denoted by $\underline{\boldsymbol{f}}_l(t) \in \mathbb{R}^8$. This appendix shows that, under some modeling assumptions, these actuators can also be used to indirectly identify $\mathcal{T}$ using three steps. First, the FRF of $\mathcal{C}$ is measured, see, e.g., [37]. Second, a parametric model $\mathcal{C}(s)$ is fitted on the FRF to provide numerical values for the system's mass matrix $\mathbf{M}$, damping matrix $\mathbf{D}$, and stiffness matrix $\mathbf{K}$. Third, the system matrices are used to derive a parametric model describing the FRF of the transmissibility matrix $\mathcal{T}$.

The first step is to measure the FRF of $\mathcal{C}$. To this end, the actuator forces $\underline{\boldsymbol{f}}_l$ are transformed to the Cartesian coordinate frame, such that they represent three forces acting on the payload in the directions x_p, y_p, z_p, and three moments acting on the payload in the directions $\theta_{x,p}, \theta_{y,p}, \theta_{z,p}$. The transformed forces are denoted by $\boldsymbol{f}_l(t) \in \mathbb{R}^6$ and, considering again small displacements, are given by

$$\boldsymbol{f}_l(t) = \mathbf{B}\underline{\boldsymbol{f}}_l(t), \quad \mathbf{B} \in \mathbb{R}^{6\times 8}. \tag{A.1}$$

Fig. A.7 shows the measured FRF of $\mathcal{C}$. It is shown in [37] that this FRF can be measured accurately with a low bias and variance by using periodic excitations provided by $\boldsymbol{f}_l$.

The second step is to fit the measured FRF of $\mathcal{C}$ with a parametric model. In this model, the BF and payload are considered as rigid bodies. Define $\underline{\boldsymbol{x}}_p$ and $\underline{\boldsymbol{x}_b}$ as the vector with payload and BF displacements locally at each air mount, and $\boldsymbol{x}_p$ and $\boldsymbol{x}_b$ as the payload and BF displacements described in Cartesian coordinates from the CoG, see (1). Furthermore, each air mount is modeled as a combination of three springs $k_{x,i}, k_{y,i}, k_{z,i}$ and three dampers $(d_{x,i}, d_{y,i}, d_{z,i})$, with $i \in \{1,2,3,4\}$, see Fig. 1b. Each air mount generates, in all three directions $q \in \{x, y, z\}$, a reaction force $-k_{q,i}(q_{p,i} - q_{b,i}) - d_{q,i}(\dot{q}_{p,i} - \dot{q}_{b,i})$, with $q_{p,i}, q_{b,i}$ representing the local payload and BF displacements at the location of air mount i in direction q. Then, the equations of motion are derived from Newton's second law applied to all six rigid-body coordinates of the payload's CoG:

$$\mathbf{M}\ddot{\boldsymbol{x}_p}(t) + \underline{\mathbf{D}\dot{\boldsymbol{x}}}_p(t) + \mathbf{K}\boldsymbol{x}_p(t) = \underline{\mathbf{D}\dot{\boldsymbol{x}}}_b(t) + \underline{\mathbf{K}\boldsymbol{x}_b}(t) + \boldsymbol{f}_l(t), \tag{A.2}$$
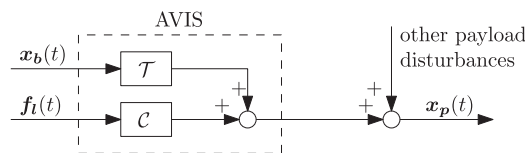
Fig. A.6. Block diagram for the AVIS. The input vectors represent BF displacements $\boldsymbol{x}_b$ and Lorentz actuator forces $\boldsymbol{f}_l$. The output vector $\boldsymbol{x}_p$ represents the payload displacements. The transfer functions $\mathcal{T}$ and $\mathcal{C}$ are called the transmissibility matrix and compliance matrix, respectively. Since the AVIS is placed on a stiff floor, and actuator forces are small, it is assumed that $\boldsymbol{x}_b$ and $\boldsymbol{f}_l$ can be considered as independent input signals.
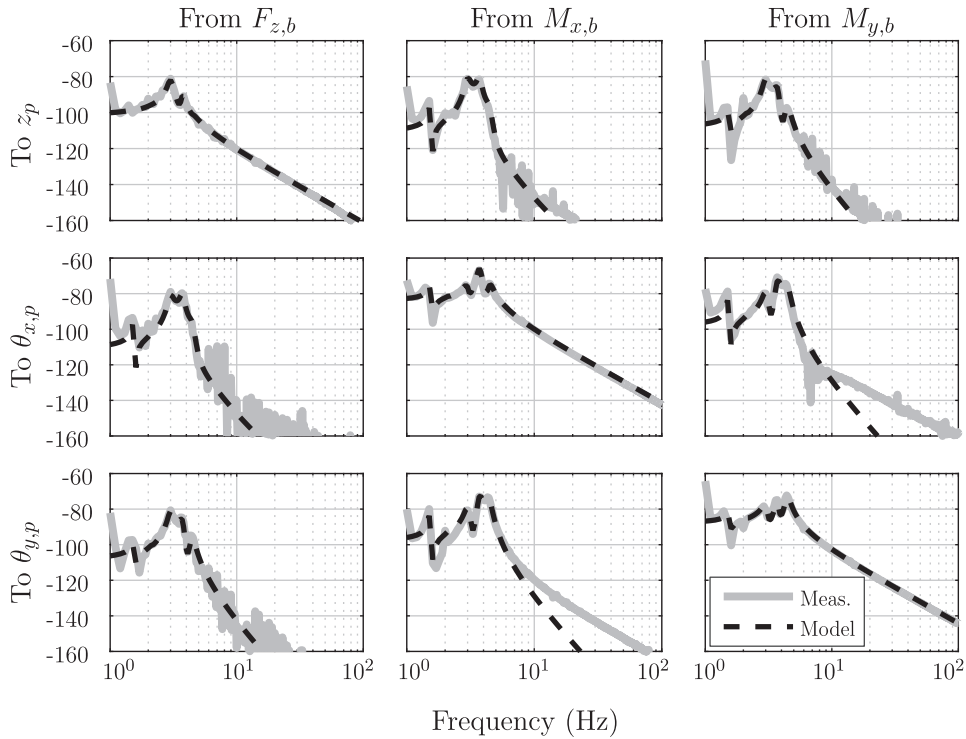
Fig. A.7. Bode magnitude plot of the compliance matrix $\mathcal{C}$. solid gray: measured FRF, dashed black: fitted parametric model.

with global mass **M**, local damping matrix $\underline{\mathbf{D}}$, and local stiffness matrix $\underline{\mathbf{K}}$ as given in Appendix D. Under the assumption that the air mounts are perfectly aligned, there exists a transformation matrix $\mathbf{T_b}$, see Appendix D, such that $\underline{\boldsymbol{x_b}} = \mathbf{T_b}\boldsymbol{x_b}$ and $\underline{\boldsymbol{x_p}} = \mathbf{T_b}\boldsymbol{x_p}$. Then, (A.2) is transformed to

$$\mathbf{M}\ddot{\boldsymbol{x}}_{\boldsymbol{p}}(t) + \mathbf{D}\dot{\boldsymbol{x}}_{\boldsymbol{p}}(t) + \mathbf{K}\boldsymbol{x}_{\boldsymbol{p}}(t) = \mathbf{D}\dot{\boldsymbol{x}}_{\boldsymbol{b}}(t) + \mathbf{K}\boldsymbol{x}_{\boldsymbol{b}}(t) + \boldsymbol{f}_{\boldsymbol{l}}(t), \tag{A.3}$$

with global damping and stiffness matrix

$$\mathbf{D} = \underline{\mathbf{D}}\mathbf{T_b}, \quad \mathbf{K} = \underline{\mathbf{K}}\mathbf{T_b}. \tag{A.4}$$

Taking the Laplace transform of (A.3),

$$(\mathbf{M}s^2 + \mathbf{D}s + \mathbf{K})\boldsymbol{X}_{\boldsymbol{p}}(s) = (\mathbf{D}s + \mathbf{K})\boldsymbol{X}_{\boldsymbol{b}}(s) + \boldsymbol{F}_{\boldsymbol{l}}(s), \tag{A.5}$$

with Laplace variable $s, \mathcal{L}\{\boldsymbol{x_b}(t)\} = \boldsymbol{X_b}(s), \mathcal{L}\{\boldsymbol{x_p}(t)\} = \boldsymbol{X_p}(s), \mathcal{L}\{\boldsymbol{f_l}(t)\} = \boldsymbol{F_l}(s)$. Recalling the definitions for $\mathcal{T}$ and $\mathcal{C}$ from Fig. A.6, parametric expressions are derived from (A.5) as

$$\mathcal{T}(s) = (\mathbf{M}s^2 + \mathbf{D}s + \mathbf{K})^{-1}(\mathbf{D}s + \mathbf{K}), \tag{A.6}$$

$$\mathcal{C}(s) = (\mathbf{M}s^2 + \mathbf{D}s + \mathbf{K})^{-1}. \tag{A.7}$$

Fig. A.7 shows a comparison between a measured FRF for $\mathcal{C}$ and a fit of the parametric model given in (A.7) for the directions (z, θ_x, θ_y). Note that, for clarity of presentation, the directions x, y, θ_z are omitted. The figure shows that the parametric model fits well at the lower frequencies where the model assumptions are valid. In the figure, three vertical suspension modes of the AVIS are visible in the frequency range 3–5 Hz. The system shows good decoupling for frequencies beyond the suspension frequencies (>5 Hz). At 1.5 Hz, a horizontal suspension mode is visible due to a small cross-coupling effect in the AVIS between the horizontal force inputs and the vertical payload motion.

The third step is to calculate the modeled FRF $\mathcal{T}(j\omega)$ which can be obtained for every frequency ω by substitution of $s = j\omega$ in (A.6). Note that this lumped-element model does not include higher-order dynamics due to limited BF and payload stiffness. Moreover, the model does not include higher-order dynamics due to non-perfect air mounts. Therefore, the modeled FRF is expected to be valid only at low frequencies, and definitely not sufficient for the main goal of this paper as described in Section 3.

Remark 7. By using the same coordinate system for x_b and x_p, the transmissibility matrix reduces to an identity matrix at very low frequencies, i.e. $\mathcal{T} \to \mathbf{I}_6$. Indeed, at low frequencies the complete system behaves as a single rigid-body such that $x_b = x_p$. This result follows immediately from (A.6) by substitution of $s = j\omega$, and taking the limit for $\omega \to 0$.

Appendix B. Proof of Eq. (19)

Using the definition of $\widetilde{\mathbf{Q}}$ from (16), its power spectrum can be written as

$$\widehat{\mathbf{S}}_{\widetilde{\mathbf{Q}}\widetilde{\mathbf{Q}}}(\omega) = \widetilde{\mathbf{T}}_{\mathbf{Q}}^H(\omega)\widehat{\mathbf{S}}_{U_1 U_1}(\omega)\widetilde{\mathbf{T}}_{\mathbf{Q}}(\omega) + \widetilde{\mathbf{T}}_{\mathbf{Q}}^H(\omega)\widehat{\mathbf{S}}_{U_1 M_U}(\omega)\widetilde{\mathbf{T}}_{\mathbf{Q}}(\omega) + \widetilde{\mathbf{T}}_{\mathbf{Q}}^H(\omega)\widehat{\mathbf{S}}_{M_U U_1}(\omega)\widetilde{\mathbf{T}}_{\mathbf{Q}}(\omega) + \widetilde{\mathbf{T}}_{\mathbf{Q}}^H(\omega)\widehat{\mathbf{C}}_{U_1 U_1}(\omega)\widetilde{\mathbf{T}}_{\mathbf{Q}}(\omega). \tag{B.1}$$

By definition of the EVD in (15), $\widetilde{\mathbf{Q}}$ has a diagonal power spectrum $\widehat{\mathbf{S}}_{\widetilde{\mathbf{Q}}\widetilde{\mathbf{Q}}} = \mathbf{\Lambda}$. Under Assumption 3 such that U_1 and M_U are uncorrelated, it follows that $\widehat{\mathbf{S}}_{U_1 M_U}$ and $\widehat{\mathbf{S}}_{M_U U_1}$ asymptotically converge almost sure to zero for $M \to \infty$. Under Assumption 6, it holds that $\mathbf{C}_{U_1 U_1} \to \sigma_{acc}^2 \mathbf{I}_{n_u}$. Moreover, $\widetilde{\mathbf{T}}_{\mathbf{Q}}\widetilde{\mathbf{T}}_{\mathbf{Q}}^H = \mathbf{I}_{n_u}$ because $\widetilde{\mathbf{T}}_{\mathbf{Q}}$ is a unitary matrix, see (15). Then, (B.1) reduces to

$$\widetilde{\mathbf{\Lambda}}(\omega) = \mathbf{\Lambda}(\omega) + \sigma_{acc}^2(\omega)\mathbf{I}_{n_u}, \quad \text{with} \quad \mathbf{\Lambda}(\omega) = \widetilde{\mathbf{T}}_{\mathbf{Q}}^H(\omega)\widehat{\mathbf{S}}_{U_1 U_1}(\omega)\widetilde{\mathbf{T}}_{\mathbf{Q}}(\omega). \tag{B.2}$$

Since $\widetilde{\mathbf{\Lambda}}$ is a diagonal matrix by the grace of (15), and $\sigma_{acc}^2 \mathbf{I}_{n_u}$ is a diagonal matrix, it follows from (B.2) that $\mathbf{\Lambda}$ must be a diagonal matrix. In other words, the noise-free power spectrum $\widehat{\mathbf{S}}_{U_1 U_1}(\omega)$ must have an EVD that equals $\widehat{\mathbf{S}}_{U_1 U_1} = \widetilde{\mathbf{T}}_{\mathbf{Q}}\mathbf{\Lambda}\widetilde{\mathbf{T}}_{\mathbf{Q}}^H$, hence the eigenvectors of the noisy and noise-free principal components coincide. Moreover, since (B.2) represents a set of decoupled equations, it follows that for $M \to \infty$ the spectral power of the ith principal component is given by

$$\mathbb{E}\left[\widetilde{Q}_i(\omega)\widetilde{Q}_i^H(\omega)\right] = \tilde{\lambda}_i(\omega) = \lambda_i(\omega) + \sigma_{acc}^2(\omega), \tag{B.3}$$

with noise-free spectral power λ_i. Then, the SNR is given by the total power $\tilde{\lambda}_i$ divided by the noise power σ_{acc}^2, which results in (17) and which completes the proof.

Appendix C. Derivation of required input power for low variance

This section derives requirements for the spectral input power to obtain a sufficiently low variance of the FRF. Recall the expression for the covariance matrix from (13), and note that, when using local sensor coordinates, this variance is given by

$$\text{Cov}(\text{vec}(\hat{\mathcal{T}}_l(j\omega))) = \frac{1}{M}(\widehat{\mathbf{S}}_{\widetilde{U}_1 \widetilde{U}_1}^{-1}(\omega))^T \otimes \widehat{\mathbf{C}}_{Y_1}(\omega). \tag{C.1}$$

Under the assumption that $n_y = n_u$, the input is measured free of noise, and the output covariance matrix is given by $\mathbf{C}_{Y_1 Y_1}(\omega) = \sigma_{acc,y}^2(\omega)\mathbf{I}_{n_u}$ (similar to Assumption 6), it follows that the covariance matrix has n_u unique singular values given by

$$\sigma_i\left(\text{Cov}(\text{vec}(\hat{\mathcal{T}}_l(j\omega)))\right) = \sigma_i\left(\frac{\sigma_{acc,y}^2(\omega)}{M}(\widehat{\mathbf{S}}_{\widetilde{U}_1 \widetilde{U}_1}^{-1}(\omega))^T\right), \quad i \in \{1, \ldots, n_u\}. \tag{C.2}$$

This can be rewritten to

$$\sigma_i\left(\text{Cov}(\text{vec}(\hat{\mathcal{T}}_l(j\omega)))\right) = \frac{\sigma_{acc,y}^2(\omega)}{M}\frac{1}{\sigma_i\left(\widehat{\mathbf{S}}_{\widetilde{U}_1 \widetilde{U}_1}(\omega)\right)}, \quad i \in \{1, \ldots, n_u\}. \tag{C.3}$$

Next, an upper bound on the variance is defined as $\sigma_i\left(\text{Cov}(\text{vec}(\hat{\mathcal{T}}_l(j\omega)))\right) \leqslant (\text{VARmax})\varsigma^2(\omega)$ for all $i \in \{1, \ldots, n_u\}$. Here, $(\text{VAR}_{max}) \in \mathbb{R}$ is user-defined and gives the allowed variance relative to ς which is the lowest singluar value of $\mathcal{T}_l = \mathbf{T}_y^{-1}\mathcal{T}\mathbf{T}_u$ representing the transmissibility matrix in local sensor coordinates, i.e. from U_1 to Y_1. Substitution of this upper bound in (C.4), the following condition regarding the input spectral power is obtained:

$$\sigma_i\left(\widehat{\mathbf{S}}_{\widetilde{U}_1 \widetilde{U}_1}(\omega)\right) \geqslant \frac{\sigma_{acc,y}^2(\omega)}{M}\frac{1}{(\text{VARmax})\varsigma^2(\omega)}, \quad \forall i. \tag{C.4}$$

Since $\widehat{\mathbf{S}}_{\widetilde{U}_1 \widetilde{U}_1}$ is a hermitian matrix ($\mathbf{A} = \mathbf{A}^H$), the singular values are identical to the eigenvalues $\tilde{\lambda}_i$ that would be obtained from an eigenvalue decomposition. Therefore, (C.4) can also be written as

$$\tilde{\lambda}_i(\widehat{\mathbf{S}}_{\widetilde{U}_1 \widetilde{U}_1}(\omega)) \geqslant \frac{1}{M}\frac{\sigma_{acc,y}^2(\omega)}{(\text{VARmax})\varsigma^2(\omega)}, \quad \forall i. \tag{C.5}$$

with $\tilde{\lambda}_i$ the eigenvalues of $\widehat{\mathbf{S}}_{\widetilde{U}_1 \widetilde{U}_1}$ which correspond with the spectral powers of the principal components.

Appendix D. Matrices and vectors for the parametric model

This appendix presents the matrices and vectors for the parametric model, where numerical values for the used parameters can be found in Table A.1.

$$\underline{x_m} = \begin{bmatrix} x_{m,1} & y_{m,1} & z_{m,1} & x_{m,2} & y_{m,2} & z_{m,2} & x_{m,3} & y_{m,3} & z_{m,3} & x_{m,4} & y_{m,4} & z_{m,4} \end{bmatrix}$$

$$\underline{x_b} = \begin{bmatrix} x_{b,1} & y_{b,1} & z_{b,1} & x_{b,2} & y_{b,2} & z_{b,2} & x_{b,3} & y_{b,3} & z_{b,3} & x_{b,4} & y_{b,4} & z_{b,4} \end{bmatrix}$$

$$\boldsymbol{x_m} = \begin{bmatrix} x_m & y_m & z_m & \theta_{m,x} & \theta_{m,y} & \theta_{m,z} \end{bmatrix}$$

$$\boldsymbol{x_b} = \begin{bmatrix} x_b & y_b & z_b & \theta_{b,x} & \theta_{b,y} & \theta_{b,z} \end{bmatrix}$$

$$\mathbf{M} = \begin{bmatrix} m & 0 & 0 & 0 & 0 & 0 \\ 0 & m & 0 & 0 & 0 & 0 \\ 0 & 0 & m & 0 & 0 & 0 \\ 0 & 0 & 0 & J_{xx} & 0 & 0 \\ 0 & 0 & 0 & 0 & J_{yy} & 0 \\ 0 & 0 & 0 & 0 & 0 & J_{zz} \end{bmatrix}$$

$$\underline{\mathbf{D}} = \begin{bmatrix} d_{1x} & 0 & 0 & d_{2x} & 0 & 0 & d_{3x} & 0 & 0 & d_{4x} & 0 & 0 \\ 0 & d_{1y} & 0 & 0 & d_{2y} & 0 & 0 & d_{3y} & 0 & 0 & d_{4y} & 0 \\ 0 & 0 & d_{1z} & 0 & 0 & d_{2z} & 0 & 0 & d_{3z} & 0 & 0 & d_{4z} \\ 0 & h_z d_{1y} & h_y d_{1z} & 0 & h_z d_{2y} & -h_y d_{2z} & 0 & h_z d_{3y} & -h_y d_{3z} & 0 & h_z d_{4y} & h_y d_{4z} \\ -h_z d_{1x} & 0 & -h_x d_{1z} & -h_z d_{2x} & 0 & -h_x d_{2z} & -h_z d_{3x} & 0 & h_x d_{3z} & -h_z d_{4x} & 0 & h_x d_{4z} \\ -h_y d_{1x} & h_x d_{1y} & 0 & h_y d_{2x} & h_x d_{2y} & 0 & h_y d_{3x} & -h_x d_{3y} & 0 & -h_y d_{4x} & -h_x d_{4y} & 0 \end{bmatrix}$$

$$\underline{\mathbf{K}} = \begin{bmatrix} k_{1x} & 0 & 0 & k_{2x} & 0 & 0 & k_{3x} & 0 & 0 & k_{4x} & 0 & 0 \\ 0 & k_{1y} & 0 & 0 & k_{2y} & 0 & 0 & k_{3y} & 0 & 0 & k_{4y} & 0 \\ 0 & 0 & k_{1z} & 0 & 0 & k_{2z} & 0 & 0 & k_{3z} & 0 & 0 & k_{4z} \\ 0 & h_z k_{1y} & h_y k_{1z} & 0 & h_z k_{2y} & -h_y k_{2z} & 0 & h_z k_{3y} & -h_y k_{3z} & 0 & h_z k_{4y} & h_y k_{4z} \\ -h_z k_{1x} & 0 & -h_x k_{1z} & -h_z k_{2x} & 0 & -h_x k_{2z} & -h_z k_{3x} & 0 & h_x k_{3z} & -h_z k_{4x} & 0 & h_x k_{4z} \\ -h_y k_{1x} & h_x k_{1y} & 0 & h_y k_{2x} & h_x k_{2y} & 0 & h_y k_{3x} & -h_x k_{3y} & 0 & -h_y k_{4x} & -h_x k_{4y} & 0 \end{bmatrix}$$

$$\mathbf{T_b} = \begin{bmatrix} 1 & 0 & 0 & 0 & -h_z & -h_y \\ 0 & 1 & 0 & +h_z & 0 & +h_x \\ 0 & 0 & 1 & +h_y & -h_x & 0 \\ 1 & 0 & 0 & 0 & -h_z & +h_y \\ 0 & 1 & 0 & +h_z & 0 & +h_x \\ 0 & 0 & 1 & -h_y & -h_x & 0 \\ 1 & 0 & 0 & 0 & -h_z & +h_y \\ 0 & 1 & 0 & +h_z & 0 & -h_x \\ 0 & 0 & 1 & -h_y & +h_x & 0 \\ 1 & 0 & 0 & 0 & -h_z & -h_y \\ 0 & 1 & 0 & +h_z & 0 & -h_x \\ 0 & 0 & 1 & +h_y & +h_x & 0 \end{bmatrix}$$

Table A.1
Model parameters of the six-axis vibration isolator.

k_{1x}	8455	N/m	k_{2x}	6476	N/m	k_{3x}	6476	N/m	k_{4x}	8455	N/m
k_{1y}	7824	N/m	k_{2y}	7824	N/m	k_{3y}	6757	N/m	k_{4y}	6757	N/m
k_{1z}	39574	N/m	k_{2z}	30376	N/m	k_{3z}	33131	N/m	k_{4z}	15401	N/m
d_{1x}	33	N s/m	d_{2x}	12	N s/m	d_{3x}	12	N s/m	d_{4x}	33	N s/m
d_{1y}	48	N s/m	d_{2y}	48	N s/m	d_{3y}	14	N s/m	d_{4y}	14	N s/m
d_{1z}	173	N s/m	d_{2z}	79	N s/m	d_{3z}	70	N s/m	d_{4z}	110	N s/m
J_{xx}	30	kg m^2	h_x	0.475	m						
J_{yy}	41	kg m^2	h_y	0.375	m						
J_{zz}	60	kg m^2	h_z	0.185	m						
m	289	kg									

References

[1] M. Heertjes, I. Sahin, N. van de Wouw, W. Heemels, Switching control in vibration isolation systems, IEEE Trans. Contr. Syst. Technol. 21 (3) (2013) 626–635.
[2] K. Iwaya, R. Shimizu, T. Hashizume, T. Hitosugi, Systematic analyses of vibration noise of a vibration isolation system for high-resolution scanning tunneling microscopes, Rev. Sci. Instrum. 82 (8) (2011) 083702.
[3] S. Ito, D. Neyer, S. Pirker, J. Steininger, G. Schitter, Atomic force microscopy using voice coil actuators for vibration isolation, in: 2015 IEEE International Conference on Advanced Intelligent Mechatronics (AIM), IEEE, 2015, pp. 470–475.
[4] L. Van De Ridder, M. Beijen, W. Hakvoort, J. Van Dijk, J. Lötters, A. de Boer, Active vibration isolation feedback control for coriolis mass-flow meters, Contr. Eng. Pract. 33 (2014) 76–83.
[5] F. Matichard et al, instrumentation and performance, Class. Quant. Grav. 32 (18) (2015) 185003.
[6] A. Preumont, M. Horodinca, I. Romanescu, B. De Marneffe, M. Avraam, A. Deraemaeker, F. Bossens, A. Abu Hanieh, A six-axis single-stage active vibration isolator based on Stewart platform, J. Sound Vib. 300 (3) (2007) 644–661.
[7] G. Hauge, M. Campbell, Sensors and control of a space-based six-axis vibration isolation system, J. Sound Vib. 269 (3) (2004) 913–931.
[8] E. Reynders, System identification methods for (operational) modal analysis: review and comparison, Arch. Comput. Methods Eng. 19 (1) (2012) 51–124.
[9] W. Weijtjens, G. De Sitter, C. Devriendt, P. Guillaume, Operational modal parameter estimation of MIMO systems using transmissibility functions, Automatica 50 (2) (2014) 559–564.
[10] P. Gajdatsy, K. Janssens, W. Desmet, H. Van Der Auweraer, Application of the transmissibility concept in transfer path analysis, Mech. Syst. Sign. Process. 24 (7) (2010) 1963–1976.
[11] M.V. van der Seijs, D. de Klerk, D.J. Rixen, General framework for transfer path analysis: History, theory and classification of techniques, Mech. Syst. Sign. Process. 68 (2016) 217–244.
[12] G. Balik, B. Caron, J. Allibe, A. Badel, J.-P. Baud, L. Brunetti, G. Deleglise, A. Jeremie, R. Le Breton, S. Vilalte, Sub-nanometer active seismic isolator control, J. Intell. Mater. Syst. Struct. 24 (15) (2013) 1785–1795.
[13] M. Beijen, D. Tjepkema, J. Van Dijk, Two-sensor control in active vibration isolation using hard mounts, Contr. Eng. Pract. 26 (2014) 82–90.
[14] M. McMickell, T. Kreider, E. Hansen, T. Davis, M. Gonzalez, Optical payload isolation using the miniature vibration isolation system (MVIS-II), in: The 14th International Symposium on: Smart Structures and Materials & Nondestructive Evaluation and Health Monitoring, International Society for Optics and Photonics, 2007, pp. 652703-1–652703-13.
[15] R. Pintelon, J. Schoukens, System Identification: A Frequency Domain Approach, John Wiley and Sons, 2012.
[16] M. Annergren, C. Larsson, H. Hjalmarsson, X. Bombois, B. Wahlberg, Application-oriented input design in system identification: optimal input design for control [applications of control], IEEE Contr. Syst. 37 (2) (2017) 31–56.
[17] Y. Shin, K. Kim, Performance enhancement of pneumatic vibration isolation tables in low frequency range by time delay control, J. Sound Vib. 321 (3) (2009) 537–553.
[18] R. Pintelon, J. Schoukens, G. Vandersteen, K. Barbé, Estimation of nonparametric noise and FRF models for multivariable systems – Part I: Theory, Mech. Syst. Sign. Process. 24 (3) (2010) 573–595.
[19] Q. Leclère, N. Roozen, C. Sandier, On the use of the H_s estimator for the experimental assessment of transmissibility matrices, Mech. Syst. Sign. Process. 43 (1) (2014) 237–245.
[20] T. Söderström, System identification for the errors-in-variables problem, Trans. Inst. Meas. Contr. 34 (7) (2012) 780–792.
[21] E. Zhang, R. Pintelon, Errors-in-variables identification of dynamic systems in general cases, IFAC-Pap. OnLine 48 (28) (2015) 309–313.
[22] J. Agüero, G. Goodwin, Identifiability of errors in variables dynamic systems, Automatica 44 (2) (2008) 371–382.
[23] R. Pintelon, J. Schoukens, G. Vandersteen, K. Barbé, Estimation of nonparametric noise and FRF models for multivariable systems – Part II: Extensions, applications, Mech. Syst. Sign. Process. 24 (3) (2010) 596–616.
[24] M. Dorosti, R. Fey, M. Heertjes, M. van de Wal, H. Nijmeijer, Finite element model reduction and model updating of structures for control, IFAC Proc. 47 (3) (2014) 4517–4522.
[25] S. Voormeeren, D. De Klerk, D. Rixen, Uncertainty quantification in experimental frequency based substructuring, Mech. Syst. Sign. Process. 24 (1) (2010) 106–118.
[26] D. Nicgorski, P. Avitabile, Conditioning of FRF measurements for use with frequency based substructuring, Mech. Syst. Sign. Process. 24 (2) (2010) 340–351.
[27] Y. Zhang, A. Alleyne, D. Zheng, A hybrid control strategy for active vibration isolation with electrohydraulic actuators, Contr. Eng. Pract. 13 (3) (2005) 279–289.
[28] D. Tjepkema, J. van Dijk, H. Soemers, Sensor fusion for active vibration isolation in precision equipment, J. Sound Vib. 331 (4) (2011) 735–749.
[29] M. Beijen, M. Heertjes, H. Butler, Self-tuning disturbance feedforward control with drift prevention for air mount systems, in: Proceedings of the Multi-Conference on Systems and Control, Sydney, NSW, Australia, 2015, pp. 400–405.
[30] M. Beijen, M. Heertjes, R. Voorhoeve, T. Oomen, Evaluating performance of multivariable vibration isolators: A frequency domain identification approach applied to an industrial AVIS, in: Proceedings of the American Control Conference, Seattle, WA, USA, 2017, pp. 3512–3517.
[31] J. Bendat, A. Piersol, Engineering Applications of Correlation and Spectral Analysis, Wiley-Interscience, New York, 1980.
[32] E. Wernholt, S. Gunnarsson, Analysis of methods for multivariable frequency response function estimation in closed loop, in: 46th IEEE Conference on Decision and Control, IEEE, 2007, pp. 4881–4888.
[33] M. Tan, J. Hammond, A non-parametric approach for linear system identification using principal component analysis, Mech. Syst. Sign. Process. 21 (4) (2007) 1576–1600.
[34] P. White, W. Collis, Analysis of the TLS frequency response function estimator, in: Proceedings of the Ninth IEEE SP Workshop on Statistical Signal and Array Processing, IEEE, 1998, pp. 156–159.
[35] C.R. Rojas, J.S. Welsh, G.C. Goodwin, A receding horizon algorithm to generate binary signals with a prescribed autocovariance, in: Proceedings of the American Control Conference, IEEE, 2007, pp. 122–127.
[36] M. Boerlage, B. de Jager, M. Steinbuch, Control relevant blind identification of disturbances with application to a multivariable active vibration isolation platform, IEEE Trans. Contr. Syst. Technol. 18 (2) (2010) 393–404.
[37] R. Voorhoeve, A. Van Rietschoten, E. Geerardyn, T. Oomen, Identification of high-tech motion systems: an active vibration isolation benchmark, IFAC-Pap. OnLine 48 (28) (2015) 1250–1255.